## PAPER

Check for updates

# Dynamics of a self-interacting sheet in shear flow†

William T. Funkenbusch, [ID] Kevin S. Silmore [ID] and Patrick S. Doyle [ID] *

Solution processing of 2D materials such as graphene is important for applications thereof, yet a complete fundamental understanding of how 2D materials behave dynamically in solution is lacking. Here, we extend previous work by Silmore *et al.*, *Soft Matter*, 2021, **17(18)**, 4707−4718 by adding short-ranged Lennard−Jones interactions to 2D sheets in shear flow. We find that the addition of these interactions allows for a rich landscape of conformations which depend on the balance between shear strength, bending rigidity, and interaction strength as well as the initial configuration of the sheet. We explore this conformational space and classify sheets as flat, tumbling, 1D folded, or 2D folded based on their conformational properties. We use kinetic and energetic arguments to explain why sheets adopt certain conformations within the folded regime. Finally, we calculate the stresslet and find that, even in the absence of thermal fluctuations and multiple sheet interactions, shear-thinning followed by shear-thickening behavior can appear.

## 1 Introduction

Solution processing and liquid exfoliation are important aspects of the production and application of 2D materials such as graphene, graphene oxide, transition metal dichalcogenides, and, more recently, 2D polymers,[1–19] but fundamental understanding of many properties of suspended 2D sheets is lacking. For example, much work has been devoted to the transition from a flat to a crumpled state with increasing temperature,[20–28] but there is still debate as to whether self-avoiding sheets crumple or are flat at all temperatures.[29–42] The introduction of attractive interactions, which appear in real systems in the form of, for example, dispersion forces, has been explored as a potential way to induce conformational changes in sheets,[36,43,44] and a series of folding transitions have also been theorized and observed in thermal simulations.[45]

One can also apply a flow field to sheets, resulting in dynamics which are even less well understood than the equilibrium behavior. Xu and Green studied the rotation of semi-flexible sheets under shear and extensional flows and found shear-thinning rheological behavior.[46,47] Yu and Graham found coil-stretch-like and compact-stretched transitions for stiff sheets in extensional flows.[48,49] They found that flexible sheets in extensional flows additionally exhibit wrinkling which significantly modifies the aforementioned transitions. Salussolia

and Botto characterized the separation of multi-sheet systems (although in 2D) with long- and short-range hydrodynamics in shear and found that separating sheets can reassemble under certain conditions.[50] Recently, Perrin and Botto also showed (again in 2D) that, despite multi-layer sheets having a higher bending rigidity than single-layer sheets,[51] a lateral hydrodynamic force at moderate sheet separations can cause the sheets to bend for shear rates much lower than expected.[52]

Previous work by Silmore *et al.*[53,54] showed that Jeffery's equations for the rotation of rigid ellipsoids in shear[55] matched well with the behavior of semi-flexible sheets in shear under certain conditions.[53] Introducing thermal energy resulted in shear-thinning followed by shear-thickening rheological behavior[54] which has been observed in dilute graphene suspensions[56] as well as dilute graphene oxide suspensions.[57] These experiments showed the same stronger shear-thinning at higher temperatures. Because these simulations involved only single sheets, they show that conformational changes may contribute to this non-monotonic rheological behavior in addition to sheet-sheet interactions (*e.g.* the buildup and breakdown of agglomerates or the formation of lamellar layers).

In many real systems, however, such as graphene, bending rigidity is several orders of magnitude greater than thermal energy[58,59] (graphene oxide being an exception, with bending rigidity about the same as thermal energy at room temperature[60]). This raises the question as to whether non-monotonic rheological behavior can be generated in the athermal limit. As discussed earlier, self-interactions are a potential method of producing conformational changes in sheets, which can affect their rheological properties.

*Massachusetts Institute of Technology Department of Chemical Engineering, 25 Ames St, Cambridge MA, 02139, USA. E-mail: pdoyle@mit.edu*

† Electronic supplementary information (ESI) available: Includes videos of notable sheet behaviors and histograms of gyration tensor eigenvalues. See DOI: https://doi.org/10.1039/d4sm00197d

In this work, we study athermal, semi-flexible sheets with long-range hydrodynamics using the model developed in previous work[53] but with the addition of attractive self-interactions. We show that single sheets with attractive self-interactions can exhibit diverse and interesting conformational and rotational behaviors. The parameters in the system allow us to define two dimensionless groups which map out the conformational space, showing several distinct regions of different conformational behaviors. These behaviors, together with rotation, give rise to non-monotonic rheological behavior. We use kinetic and energetic arguments to explain our results.

## 2 Models and methods

### 2.1 Simulation method

Similar to the model employed in previous work,[53,54] we construct hexagonal sheets with circumradius $L = 39a$ with beads of radius $a$ such that each interior bead has 6 tangent neighbors, totalling $N = 1141$ beads. We also apply many of the same forces to beads within the sheets. We use harmonic forces between neighboring beads with in-plane stiffness $k$ and dihedral forces between neighboring triangles of beads with bending rigidity (out-of-plane stiffness) $\kappa$. This discrete bending rigidity can be mapped to a continuum bending rigidity, $\tilde{\kappa}$, with $\tilde{\kappa} = \kappa/\sqrt{3}$ for this specific triangulation.[61] We set the in-plane stiffness of the sheets to be much larger than their out-of-plane stiffness, as in true in many real system. This can be quantified using the Föppl–von Kármán number, FvK $\sim kL^2/\kappa$, which was between $10^3$ and $10^7$ for the simulations in this paper. Thus, the sheets are inextensible relative to bending. We also apply hard-sphere interactions between non-neighboring beads with a pair-potential which places overlapping beads tangent to each other under Rotne–Prager–Yamakawa dynamics, which give long-range hydrodynamics (see below).

Finally, we apply a short-ranged interaction in the form of a truncated Lennard–Jones potential between non-neighboring beads:

$$U_{\text{LJ}}(r) = 4\varepsilon\left[\left(\frac{\sigma}{r}\right)^{12} - \left(\frac{\sigma}{r}\right)^6\right], \tag{1}$$

where $\varepsilon$ is the interaction strength and $\sigma$ is the interaction range. We use a turn-on distance of $r_{\text{on}} = 2a$ and cut-off radius of $r_{\text{cut}} = 2.5\sigma$. For all simulations, we set $\sigma = 4\sqrt{6}a/3$.

Beads can interact via this potential along the sheet surface, which may change the in-plane behavior of the sheets. However, we find empirically that, even for the largest interaction strengths used, the harmonic bonds between neighboring beads in a flat sheet extend by less than 0.1% of their equilibrium distance. Therefore, we expect that self-interactions do not significantly affect the in-plane interactions of the sheet.

We integrate this system forward in time using an Euler–Maruyama integrator with the following equations of motion

for Brownian dynamics with hydrodynamics:

$$d\mathbf{x}_i = \left(-\sum_j \mathcal{M}_{ij}\frac{\partial U_i}{\partial \mathbf{x}_j} + \mathbf{L}\mathbf{x}_i\right)dt, \tag{2}$$

where $(\mathbf{L})_{mn} = \dot{\gamma}\delta_{m1}\delta_{n2}$ is the velocity gradient tensor for simple shear with shear rate $\dot{\gamma}$ and $U_i$ is the sum of the applied potentials on bead $i$. To achieve long-range hydrodynamics, we use the Rotne–Prager–Yamakawa tensor[62] for $\mathcal{M}_{ij}$, which is given analytically by

$$\mathcal{M}_{ij} = \frac{1}{6\pi\eta a}\begin{cases} \left(\frac{3a}{4r} + \frac{a^3}{2r^3}\right)\mathbf{I} + \left(\frac{3a}{4r} - \frac{3a^3}{2r^3}\right)\hat{\mathbf{r}}\hat{\mathbf{r}}^{\text{T}} & r > 2a \\ \left(1 - \frac{9}{32a}\right)\mathbf{I} + \frac{3}{32a}\hat{\mathbf{r}}\hat{\mathbf{r}}^{\text{T}} & r \leq 2a, \end{cases} \tag{3}$$

where $\hat{\mathbf{r}}$ is the unit vector pointing from particle $i$ to particle $j$.

The Rotne–Prager–Yamakawa tensor models long-range, pairwise hydrodynamic interactions between beads, with each bead acting as a regularized Stokeslet.[53] Thus, finite discretizations of these beads as sheets have some degree of permeability. However, Yu and Graham recently showed that, for similarly discretized sheets, the permeation velocity (i.e. the fluid velocity normal to the sheet surface) in extensional flows tends to be small (on the order of 1% relative to the sheet size and strain rate).[49] We expect shear flows to carry similar permeation velocities. Second, for small enough sheets, lubrication forces are relatively small compared to the forces from self-interaction. We discuss this assumption and the sheet size limit in Appendix A. Conceptually, because the applied self-interaction includes a repulsive component and equilibrium distance, small enough sheets do not approach closely enough for lubrication forces to be significant.

Initially flat sheets aligned with the flow-vorticity plane were rotated by an angle $\theta = 5°$ about the vorticity axis and then by a varying angle $\phi$ about the flow axis. We sample from $\phi = 0°$ to $\phi = 90°$ with samples at every $5°$. In averages over $\phi$, we give relative weights to each $\phi$ proportional to $\sin\phi$, corresponding to initially randomly oriented sheets. We use a time step of $\dot{\gamma}\Delta t = 2 \times 10^{-4}$ for all simulations. Simulations were run for 2000 strain cycles ($\dot{\gamma}t = 2000$) and results were calculated using the last 200 strain cycles using data from every $100\dot{\gamma}t$, as analysis of the autocorrelation of sheet properties such as the radius of gyration at small interaction strengths (i.e. for tumbling sheets, as described later, as they have the slowest decaying autocorrelations) showed that approximately every $100\dot{\gamma}t$ are independent. Simulations were run using HOOMD-blue on NVIDIA GeForce GTX 1080 Ti's[63] with a custom package from Silmore et al.[53] which was adapted from Fiore et al.[64] All images of sheets were rendered using Ovito.[65]

### 2.2 Dimensionless groups

The addition of self-interaction adds two new parameters to the system: the interaction strength, $\varepsilon$, and interaction range, $\sigma$. To give a roughly continuous energy landscape for two sheets sliding parallel to each other, we require $\sigma \gg a$. As mentioned earlier, for all sheets in this work, we choose

$\sigma = 4\sqrt{6}a/3 \approx 3.27a$. While $\varepsilon$ is the energy scale for the interaction between two beads, the energy scale for the interaction of a bead with a plane of beads separated by the equilibrium distance of $\sigma$ is

$$\tilde{\varepsilon}\sigma^2 = \varepsilon\frac{\sigma^2}{2\sqrt{3}a^2}, \tag{4}$$

where $\tilde{\varepsilon} = \varepsilon/2\sqrt{3}a^2$ is the interaction energy density of the sheet. For two parallel sheets of characteristic size $L$ aligned with the shear-vorticity plane and separated by a distance $\sigma$, shear acts as a force trying to separate the two sheets by sliding them along each other, while their interaction resists this sliding. Taking the ratio of these two forces gives a dimensionless group characterizing the ability of attractive interaction to resist shear:

$$\chi \equiv \frac{\tilde{\varepsilon}\sigma^2}{6\pi\eta\dot{\gamma}L^2\sigma}\left(\frac{L}{a}\right), \tag{5}$$

where $\eta$ is the fluid viscosity and $\dot{\gamma}$ is the shear rate. This dimensionless group characterizes the ability of nearby sections of the sheet to slide along each other. A more detailed derivation of this dimensionless quantity can be found in Appendix B.

We note the existence of the bead radius, $a$, in this dimensionless number. In previous work,[53,54] $a$ was the smallest resolvable length scale and did not play a role in the dynamics. Here, because interactions happen between individual beads, $a$ is relevant. The quantity $(L/a)$ is proportional to the number of interactions along the edge of the sheet. In a physical system, $a$ now corresponds to the interacting elements of a sheet, for example, individual carbon atoms in a graphene sheet interacting *via* van der Waals forces. Typical solution-processed sheets have sizes ranging from nanometers to micrometers[66] and may interact at a wide range of distances.[67] Further control over the shear rate in experiments means that this dimensionless number can span several orders of magnitudes, and we thus expect this dimensionless number to reveal interesting transitions in real systems.

While the ratio of bending rigidity to shear, denoted $S$ in previous work[53,54] with

$$S = \frac{\kappa}{\pi\eta\dot{\gamma}L^3}, \tag{6}$$

is a relevant dimensionless group for the dynamics of this system, as we discuss in the results, we find that another illuminating group is the ratio between bending rigidity and interaction strength:

$$K \equiv \frac{\kappa}{\tilde{\varepsilon}\sigma^2}. \tag{7}$$

Interaction tries to move sections of the sheet together by folding, while bending rigidity resists this folding. Thus, when $K \gg 1$, attraction interactions cannot overcome bending rigidity, and we expect the sheet to behave as in previous work.[53,54] This dimensionless group is also convenient because it is a function of material properties, while $\chi$ can be tuned experimentally by adjusting shear rate.

Plots varying $K$ and $\chi^{-1}$ thus have a convenient physical interpretation: moving along the first axis adjusts the material property of bending rigidity to interaction strength, while moving along the second axis changes the experimental property of shear force relative to interaction strength. The value of $S$ can be determined from the values of $\chi$, $K$, $\sigma$ and $a$ with $S = 6\chi K(a/L)(\sigma/L)$.

# 3 Conformational properties

## 3.1 Identifying sheet conformations

The conformational properties of sheets are highly sensitive to experimental conditions ($\chi$), material properties ($K$), and initial conditions (*e.g.* the initial orientation of the sheets relative to the flow axis, $\phi$). We identify four different conformations that sheets can exhibit: flat, tumbling, 1D folding, and 2D folding. An example of each is shown in Fig. 1. Videos of simulations for each conformation along with their corresponding average signed local mean curvature (see Section 3.3) are included in the ESI.† We examine how the values of $\chi$, $K$, and $\phi$ lead to each of these conformations in future sections. In this section, we show how each conformation can be characterized.

We identify these conformations by looking at the square root of the eigenvalues of the gyration tensor, $\lambda_i$ ($i = 1, 2, 3$ with $\lambda_1 > \lambda_2 > \lambda_3$), which correspond to the three characteristic lengths of the conformation. We take averages of each $\lambda_i$ over the last $250\dot{\gamma}t$ of the simulation every $0.25\dot{\gamma}t$, denoted $\bar{\lambda}_i$.

Flat sheets have almost no bends and therefore $\bar{\lambda}_1$ and $\bar{\lambda}_2$ are near their maximum value of $0.456L$ at all times. We categorize sheets as flat if $\bar{\lambda}_2 > 0.4L$. They are the only sheet conformation we observe which are not necessarily continuously rotating about the vorticity axis.

Tumbling sheets are characterized by impermanent folds which cause their $\lambda_i$ to fluctuate significantly throughout the simulation. We categorize sheets as tumbling if, regardless of $\bar{\lambda}_i$, the smallest standard deviation in $\lambda_i$ (over the last $200\dot{\gamma}t$) is greater than $7 \times 10^{-3}L$ or the largest standard deviation in $\lambda_i$ is greater than $3 \times 10^{-2}L$.

1D folded sheets are characterized by a series of parallel folds, resulting in a $\lambda_1$ close to the maximum value, but a much smaller $\lambda_2$. We categorize sheets as 1D folded when $\bar{\lambda}_1 > 0.4L$ and $\bar{\lambda}_2 < 0.4L$.

2D folded sheets are characterized by the appearance of non-parallel folds, causing $\lambda_1$ to deviate significantly from its maximum value. We categorize sheets as 2D folded when $\bar{\lambda}_1 < 0.4L$. 1D folded and 2D folded sheets are referred to together as folded sheets. Folded sheets are distinct from tumbling sheets, which also have folds, because their folds are persistent over time.

The boundaries between different sheet conformations were chosen by looking at histograms of $\bar{\lambda}_i$ and the standard deviation in $\lambda_i$, included in the ESI.† There is a clear gap in the histogram of $\bar{\lambda}_2$ at $0.4L$, making $\bar{\lambda}_2 > 0.4L$ a natural choice for characterizing a sheet as flat. The transition between 1D and 2D folded sheets appears continuous in that sheets can have both parallel and non-parallel folds. The cutoff between these
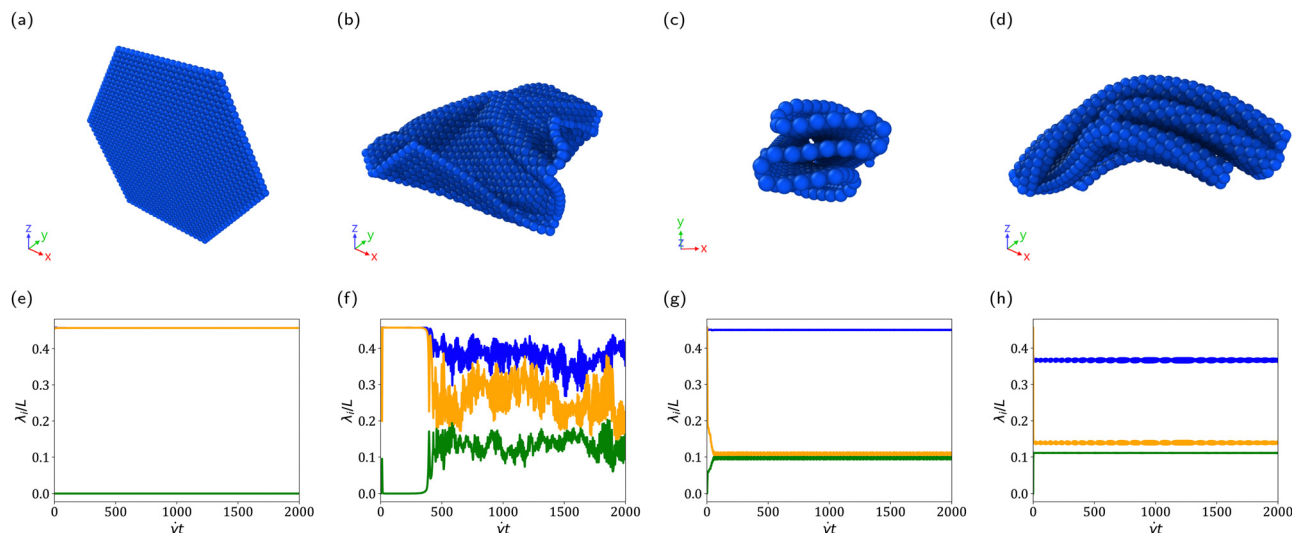
**Fig. 1** (a)–(d) Example conformations for (a) flat, (b) tumbling, (c) 1D folded, and (d) 2D folded sheets. $x$ is the flow direction and $y$ is the shear direction. (e)–(h) Square root of the eigenvalues of the gyration tensor, $\lambda_i$, over time for the (e) flat, (f) tumbling, (g) 1D folded, and (h) 2D folded sheets. Green is the smallest, orange is the second largest, and blue is the largest characteristic length.

conformations was therefore chosen by eye by finding a value of $\bar{\lambda}_1$ which seems to correspond to the beginning of the appearance of non-parallel folds. For tumbling sheets, the cutoffs were chosen again by eye such that each distribution of standard deviations for tumbling sheets appears normal-like.

### 3.2 Phase map of sheet conformations

We performed a parameter sweep across $\chi$, $K$, and $\phi$ and categorized each conformational state as flat, tumbling, 1D folded, or 2D folded. We plot using $\chi^{-1}$ instead of $\chi$ as increasing $\chi^{-1}$ corresponds to increasing shear rate, as one might see in a rheological experiment. As this is a large, 3D phase space, we present 2 slices at $\phi = 0°$ and $\phi = 45°$, shown in Fig. 2. First looking at the phase plot for $\phi = 0°$, we see clear divisions between each conformation. For large $K$ ($>1$), attractive interactions cannot overcome bending rigidity, and sheets tend to be flat. At large $\chi^{-1}$ ($>100$) and low $K$ ($\lesssim 1$), shear is able to break local attractive interactions, and the sheets tumble. At low $\chi^{-1}$ ($\lesssim 100$) and low $K$ ($\lesssim 1$), shear is unable to break local attractive interactions, so folds are permanent and the

sheets are 1D or 2D folded. Lower values of $\chi^{-1}$ at low $K$ ($<1$) correspond to less well-aligned folds and thus more 2D folded sheets.

At $\phi = 45°$, the features of the plot remain the same with one notable exception. The tumbling region expands to occupy the high $\chi^{-1}$ ($>100$), high $K$ ($>1$) regime, similar to Fig. 6 in previous work,[53] where the continuously tumbling regime was larger for larger $\phi$. The specific sheets which tumble for $K \gtrsim 1$ are unpredictable, but on average tumbling behavior is more common at larger $\phi$ and $\chi^{-1}$. This makes sense, as larger $\phi$ mean larger initial deformations from the flat conformation and larger $\chi^{-1}$ at constant $K$ mean stronger initial buckling due to a reduced value of $S$, the dimensionless ratio of bending rigidity to shear strength. However, the tumbling behaviors in the sheets in this work are notably different than in previous work[53] due to the presence of self-interaction. For example, in Fig. 3, the sheet forms several, slowly sliding folds which continuously flip in sequence. We term this "teacup" behavior. This behavior was observed for many initial orientations near the tumbling/folded boundary ($1.4 \times 10^2 \leq \chi^{-1} \leq 1.4 \times 10^3$).
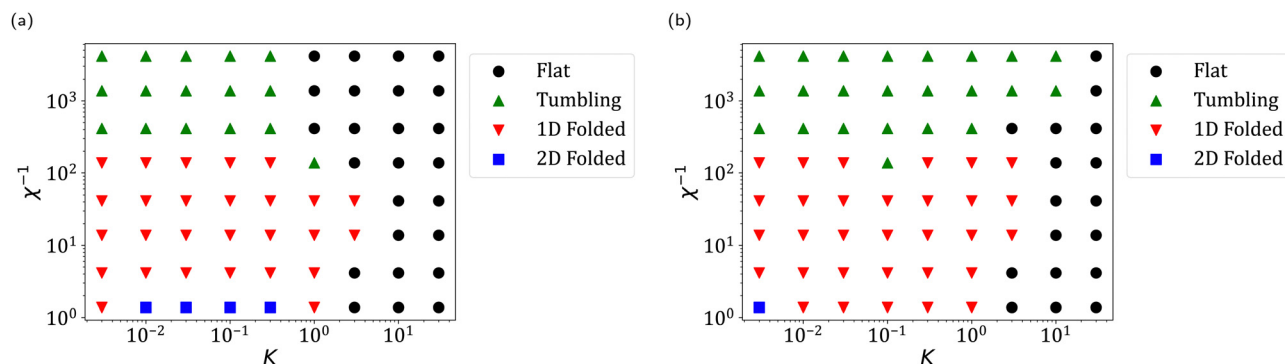


**Fig. 2** Conformational phase map of sheets with initial conditions (a) $\phi = 0°$ and (b) $\phi = 45°$.
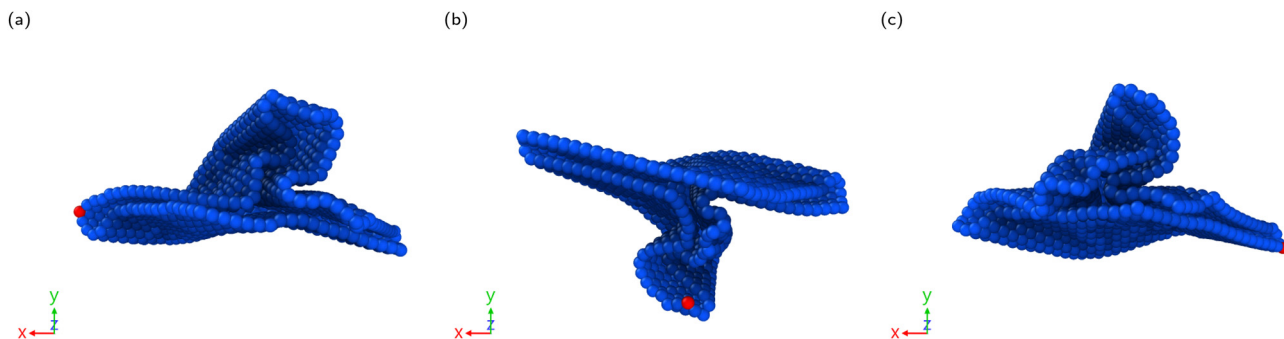
**Fig. 3** Sequential snapshots showing a 180° rotation of a sheet exhibiting teacup behavior, rotating in the counterclockwise direction with $\chi = 2.42 \times 10^{-3}$, $K = 0.01$, and $\phi = 85°$. $x$ is the flow direction and $y$ is the shear direction. A single bead is colored red to guide the eye.

Teacup behavior is usually transient in the sense that sheets alternate between it and more typical tumbling behavior over long time scales (several hundred $\dot{\gamma}t$). It is classified as tumbling due to the existence of non-persistent folds and is difficult to distinguish from typical tumbling behavior using the values of $\bar{\lambda}_i$ and the standard deviations of $\lambda_i$. A video of a simulation with this behavior is included in the ESI.†

Within a given region (flat, tumbling, and folded), sheet behavior can be predicted reliably. Near the boundaries between regions, sheet behavior may be highly sensitive to initial orientation.

### 3.3 Bending modes of 1D folded sheets

As in previous work,[53] we calculate the signed local mean curvature of the sheets and calculate the average over 101 equally spaced snapshots during the last $200\dot{\gamma}t$, giving an average signed local mean curvature (ASLMC). We plot these for the $\phi = 0°$ and $\phi = 45°$ conditions in Fig. 4. These plots correspond well to the characterizations given in the previous section. Flat sheets have no local mean curvature, and thus have an ASLMC of about 0 at all points. Tumbling sheets have significant but non-persistent folds, and their ASLMC's thus appear noisy. Folded sheets have persistent folds, and thus are characterized by sharp bands of high magnitude ASLMC. 1D folded sheets have folds which are aligned along a single axis, while 2D folded sheets have non-parallel folds which can branch off into more folds. Some sheets, especially for $\phi = 45°$ have characteristics of both 1D and 2D folded sheets.

1D folded sheets at the boundary with tumbling sheets (e.g. $\chi^{-1} = 1.4 \times 10^{2}$) typically have two close parallel folds and moderate curvature throughout the rest of the sheet. These 1D folded sheets take on a "rolled-up" conformation, as seen in Fig. 5. A video of a simulation of a rolled-up sheet is included in the ESI.† Interaction is strong enough to cause an initial folding of the sheet, but shear is strong enough to anneal all but the last two folds. This results in rolled-up sheets being an even more energetically favorable state due to the high degree of contact for self-interactions and gentle folding throughout. 1D folded sheets have a number of folds ranging from 2-folds in rolled up sheets, to 6, evenly spaced folds. There appears to be no clear pattern to the exact number of folds that will

appear, although roughly the number appears to increase with decreasing $\chi^{-1}$ unless the sheet 2D folds.

We can estimate the expected number of folds using a simple energetic argument balancing the bending and interaction energies of a 1D folded sheet, which is detailed in Appendix C. Doing so, we obtain the following estimate for the optimal number of folds, $n^{*}_{\text{fold}}$, in a rectangular 1D folded sheet:

$$n^{*}_{\text{fold}} \approx \sqrt{\frac{2L/w_{\text{fold}} + 1}{1 - \beta + \alpha K}} - 1, \tag{8}$$

where $\alpha$ and $\beta$ are fit parameters. $\alpha$ is a measure of the relative importance of bending to interaction strength and $\beta$ is a measure of the interaction energy of beads within a fold. We find $\alpha = 0.0618 \pm 0.0010$ and $\beta = 0.528 \pm 0.003$ ($\pm$ one standard deviation) for rectangular sheets. $w_{\text{fold}}$ is a correlation length characterizing the width of a fold, which is an unknown function of the system parameters, including perhaps the Föppl–von Kármán number. We observe that all folded sheets in our simulations have $w_{\text{fold}} \approx 6a$, which corresponds to the smallest fold a sheet can have. This means that folds under the conditions in this work are controlled by the smallest length scale, $a$.

For small $\chi^{-1}$ ($\lesssim 41$), shear is not strong enough to break up all the folds, and the sheet can obtain an energetically stable folded configuration. In the small $K$ limit for sheets with $L = 39a$, eqn (8) approaches about 4.46, which is close to 4, the most common number of folds observed. For sheets with $L = 79a$, eqn (8) approaches about 6.62. A series of simulations run with $L = 79a$ and $\phi = 0°$ in the 1D folded regime showed 6 folds at higher $\chi^{-1}$ (shear rates) and 8 folds at lower $\chi^{-1}$.

For slightly higher $\chi^{-1}$ ($\approx 141$), shear is strong enough to break up all but 2 folds and the sheet adopts a more energetically favorable rolled-up conformation, which is not modelled by eqn (8). At even higher $\chi^{-1}$ ($\gtrsim 410$), shear is strong enough to continuously break new folds which form as the sheet tumbles.

Because $\alpha \approx 0.05$, the number of folds predicted by eqn (8) does not decrease significantly until $K \approx 20$. The sheets flattening at about $K = 3.0$, a full order of magnitude lower, is
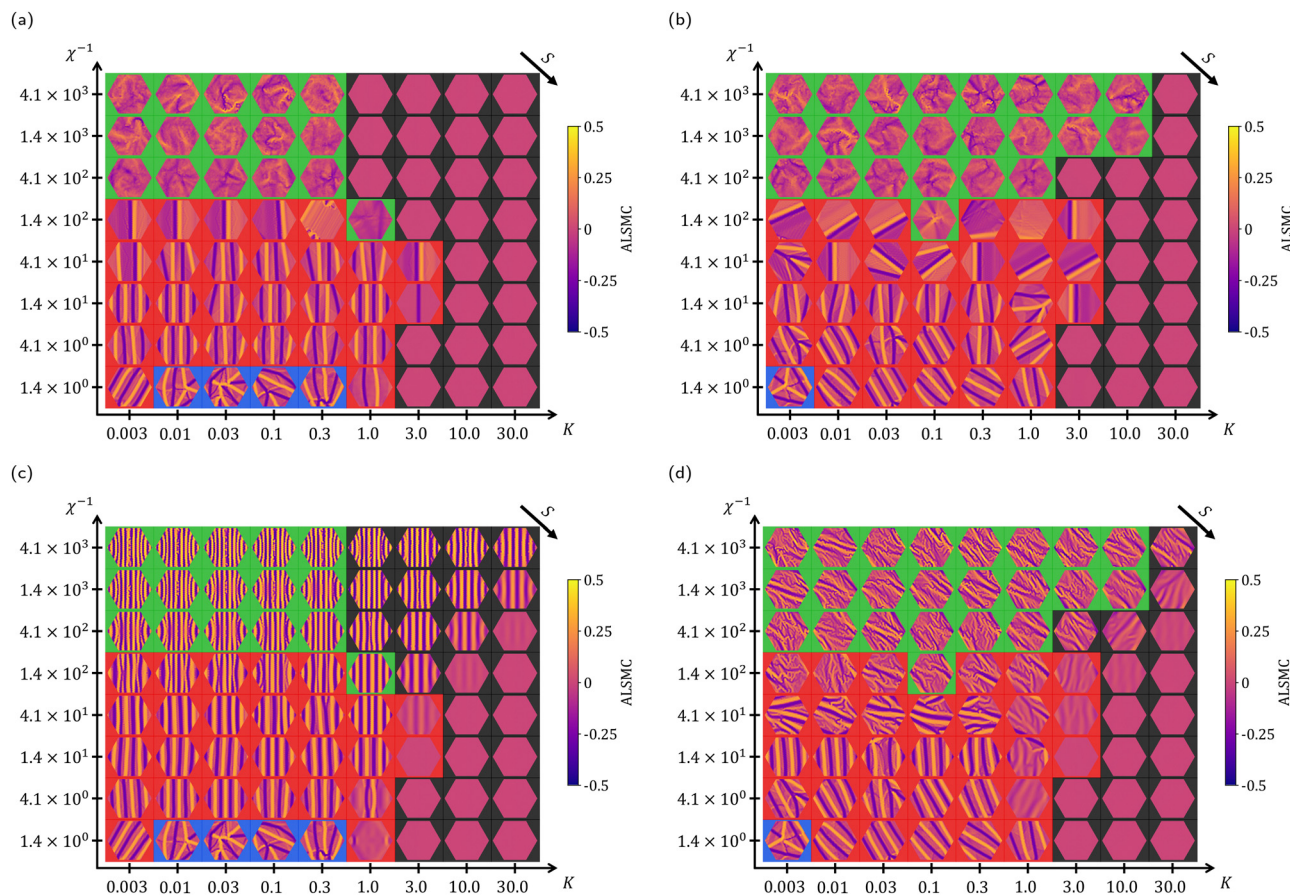
(a)

(b)

(c)

(d)

**Fig. 4** Average signed local mean curvatures for sheets during the last $200\dot{\gamma}t$ with (a) $\phi = 0°$ and (b) $\phi = 45°$. Signed local mean curvatures for sheets at their initial flip with (c) $\phi = 0°$ and (d) $\phi = 45°$. Backgrounds correspond to different conformational behaviors (black: flat, green: tumbling, red: 1D folded, blue: 2D folded). Diagonal lines running up and to the right correspond to sheets with constant $S$. Moving right or down corresponds to increasing $S$ by about a factor of 3. The arrow in the top right corner of each plot indicates the direction of maximally increasing $S$. For reference, the sheet at $K = 1.0$, $\chi^{-1} = 1.4$ has $S \times 10^5 = 920$.
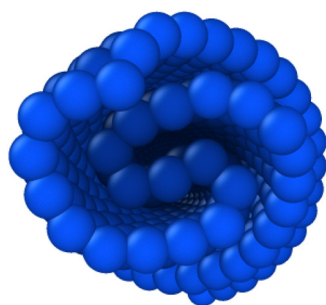
**Fig. 5** Example of a 1D folded sheet that adopts a rolled-up conformation. $x$ is the flow direction and $y$ is the shear direction.

therefore likely a kinetic phenomenon, which we explore in the next section.

### 3.4 Creation of persistent folds in 1D folded sheets

To explain why sheets in shear adopt configurations with parallel folds as opposed to other configurations (*e.g.* the

"double folded" configuration observed by Abraham and Kardar[45]), we return to previous work,[53] which calculated the buckling modes of sheets in shear as a function of the ratio of bending rigidity to shear, $S = \kappa/\pi\eta\dot{\gamma}L^3$, at $\phi = 0°$ and at the maximal in-plane stress for a flipping sheet, $\theta = 45°$. This analysis did not consider attractive interactions, which could change the buckling behavior, however we believe it to still be useful. Lines of constant $S$ correspond to lines of slope 1 in plots of $K$ *versus* $\chi^{-1}$. In our simulations, $S \times 10^5$ ranges from $9.4 \times 10^{-4}$ to $2.8 \times 10^4$, which covers more than 10 of the first buckling transitions. Notably, the calculated buckling modes from previous work[53] have alternating signs in curvature, just like what is observed in the 1D folded sheets in this work.

Fig. 4 shows the local mean curvature for sheets averaged over the last $200\dot{\gamma}t$ and during their initial flip (determined as when the average normal vector of the triangles in the sheet is closest to $\theta = 45°$). As $\chi^{-1}$ decreases for low $K$, the number of folds at the initial buckle decreases as expected because the effective bending rigidity increases relative to shear strength (given by $S$). In the 1D folded regime, sheets have folds which which are sharper in the initial buckle than the buckles that appear in the absence of interactions, showing that interaction

is strong enough to affect the initial buckling. In this regime, the number of folds often decreases from the initial buckle to the final conformation, showing annealing to a more energetically stable configuration. As $K$ increases, the magnitude of the curvature in the initial flip decreases, again due to an increasing $S$, until the sheet eventually appears flat. While the analysis done in previous work[53] was only done for sheets with $\phi = 0°$, the same trends are seen in sheets with any value of $\phi$, as seen in Fig. 4d.

We propose that persistent folds in 1D folded sheets are formed during the initial buckling of the sheet during the first flip followed by annealing caused by shear towards an energetically stable state. If shear is too strong ($\chi^{-1} \gtrsim 410$), the folds formed during buckling are not persistent, and the sheet tumbles or flattens. At an intermediate value of shear ($\chi^{-1} \approx 141$), folds form during buckling but most are broken up by shear, resulting in an energetically favorable rolled-up sheet. At lower values of shear ($\chi^{-1} \lesssim 41$), shear anneals the sheets towards their energetically preferred number of folds as predicted by eqn (8). If shear is too weak, it can only anneal partially (thus why some 1D folded sheets have more than 4 folds). Annealing can only decrease the number of folds. So, if the number of bends in the initial buckle is less than the energetically ideal number of folds, it is kinetically trapped with that number of folds. Because the buckling modes of sheets in shear have parallel folds, the resulting conformations have parallel folds.

At low $K$, interactions are stronger than buckling, so buckling will propagate into folds. For $K \gtrsim 1$, interactions are not strong enough to overcome bending, so the extent of buckling is determined by the competition between bending rigidity and shear (i.e. the value of $S$). This explains how sheets can transition from flat to 1D folded and back to flat with increasing shear at $K = 3.0$. At low shear, the sheets do not buckle strongly, and interactions are insufficient to fold the sheet. As shear increases, $S$ decreases, and the sheets buckle more strongly. Only if the buckling is strong enough can it initiate folding through interactions. Once shear becomes too strong, however, interaction is not strong enough to create persistent folds, so the sheet is flat. The critical value of $S \times 10^5$ above which sheets will not buckle if $K \sim 3$ is about 943 (which is indeed the lowest value of $S$ in these simulations above the first buckling transition determined in previous work[53]). The critical value of $\chi \times 10^5$ below which shear is too strong for sheets to fold is approximately 710.

$S = 6\chi K(a/L)(\sigma/L)$, so depending on the size of a given sheet, the 1D folded region between two flat regions may be inaccessible. Specifically, given a critical $S^*$ and $\chi^*$, we require $S < S^*$, $\chi > \chi^*$, and $K \sim 1$. As $L$ increases, $S$ decreases relative to $\chi$, and we expect the 1D folded region to increase in width. Similarly, the region decreases in width with increasing $\sigma$. Therefore, this region increases in size as the size of the sheet increases relative to interaction range. Because $\chi^* \approx S^*$, $K \sim 1$, and $(L/a) \gg 1$, this region should exist if $\sigma$ is not much larger than $L$ (if $(\sigma/L) \lesssim (1/K)(S^*/6\chi^*)(L/a)$), that is, if sheets are not much smaller than the range of their interactions. In such a system,

$\chi$ is no longer the relevant dimensionless parameter as each bead would interact with every other bead in the sheet and therefore $\tilde{\varepsilon}\sigma^2$ is no longer the relevant energy scale.

If both $\chi^{-1}$ and $K$ are small, small deviations from the alignment of the folds caused by finite-size, edge, and/or initial orientation effects will cause the spontaneous formation of more folds, and the sheet can 2D fold. This is supported by the 2D folded sheets in Fig. 4c, which are already in their 2D folded configuration at the first flip.

It is important to consider how sheet behavior would change with sheet shape. The equation for the optimal number of folds was derived for a rectangular sheet but the overall arguments are valid as long as the number of beads vertically along the folds does not change quickly across the width of the sheet (relative to the width of folded regions). This, along with the equation matching with the hexagonal sheet simulations in this work, suggest that eqn (8) is applicable for a broad range of sheet shapes with slowly changing widths.

Changing the sheet shape will affect the bending modes of the sheet and therefore the critical values of $S$ corresponding to different buckling modes. This might affect the shape of the right edge of the folded/flat boundary due to the earlier discussion of the importance of $S$. Additionally, videos of 1D folded sheets (provided in the ESI†) show that the process of a 1D folded sheet losing folds involve these folds "sliding" along the width of the sheet until it hits the edge of the sheet, where the fold disappears. This process may be affected by the shape of the sheet. Simulations with different sheet shapes (e.g. rectangular or circular) would be valuable in illuminating the effects of sheet shape on the formation and breaking of 1D folds.

## 4 Rheological properties

### 4.1 Sheet viscosity calculations

The stress of a dilute suspension of force-free rigid particles is

$$\Sigma = -p\langle I \rangle + 2\eta E^\infty + n\langle \tilde{\Sigma} \rangle, \tag{9}$$

where $p$ is the pressure, $E^\infty$ is the rate-of-strain tensor, $n$ is the number density of particles, and $\tilde{\Sigma}$ is the stresslet (the first moment of the stress on a particle).[68] As in previous work,[54] we calculate an approximate upper bound on the stresslet using the minimum-bounding ellipsoid of the sheet, its Jeffrey orbits,[55] and the stress for an ellipsoidal particle as found in Kim and Karilla.[69] The resulting average off-diagonal (flow-gradient) contribution to the stress over the last $200\dot{\gamma}t$, which is expected to grow linearly with the viscosity of a dilute suspension of these sheets, is shown in Fig. 6.

The sheet viscosity shows 2 different behaviors based on $K$. For $K \gtrsim 10.0$, sheets have a small sheet viscosity at low $\chi^{-1}$ (i.e. low shear rates). Flat sheets which rotated about the vorticity axis contributed a higher stress than flat sheets in the flow-vorticity plane, with $\tilde{\Sigma}_{12}/(6\pi\eta\dot{\gamma}L^3) > 1.5$. These sheets were ones initially oriented with their normal close to the
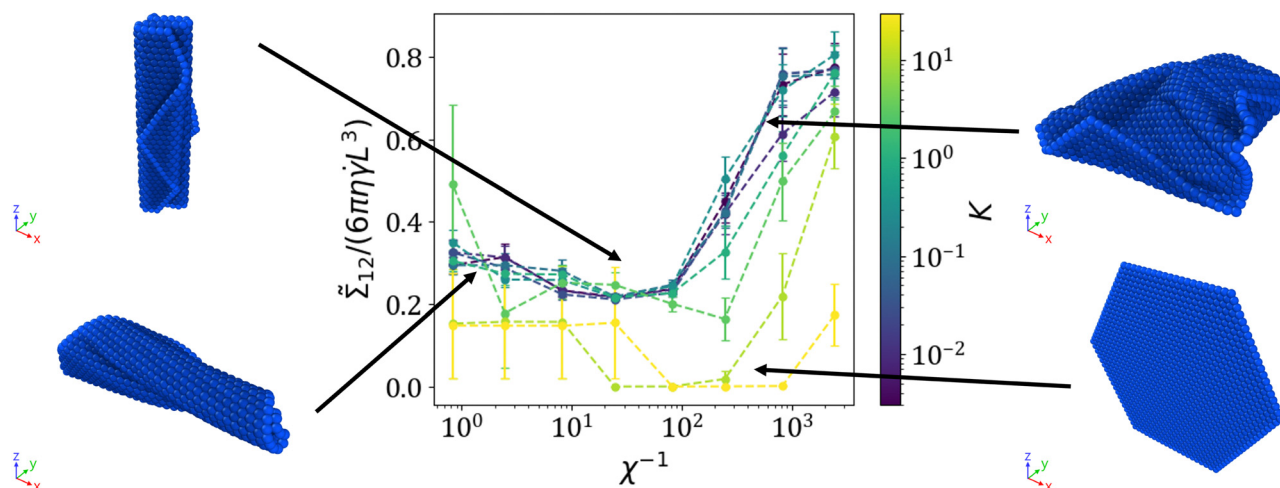
**Fig. 6** Stresslet ("sheet viscosity") averaged over the last $200\dot{\gamma}t$ and all $\phi$. Error bars are 95% confidence intervals. Dotted lines drawn to guide the eye. On the borders are characteristic behaviors for different regions. $x$ is the flow direction and $y$ is the shear direction. Top left: high alignment folded. Bottom left: low alignment folded. Top right: tumbling. Bottom right: flat.

vorticity axis ($\phi = 85°$ or $90°$). Finally, once shear is strong enough to induce tumbling, shear-thickening behavior begins.

For $K \lesssim 1.0$, there is steady shear-thinning followed by shear-thickening behavior which appears near the same critical $\chi^{-1}$ as for the high $K$ behavior. We discuss the origin of these behaviors in the next section.

### 4.2 Explanation of non-monotonic rheological properties

The nature of this shear-thinning into shear-thickening behavior is different than that with thermal energy but no interactions, which resulted from the "$u$-turn" radius of a flipping sheet.[54] In our current work, sheets in the shear-thinning regime are 1D or 2D folded.

We calculate three summary statistics, the radius of gyration, $R_g/L$, the relative shape anisotropy, $\zeta^2$, and the orientation of the largest axis of the minimum bounding ellipsoid of the sheet dotted with the vorticity axis, $|\mathbf{v}_1 \cdot \hat{z}|$, which we term the "alignment" of the sheet. The relative shape anisotropy varies from 0 to 1, with 0 occurring only if all beads are on the same line, and 1 occurring only if the beads have spherical symmetry. The alignment also varies from 0 to 1, with 0 occurring if the largest axis of the sheet is in the shear-flow plane, and 1 occurring if the largest axis of the sheet is along the vorticity axis. Scatter plots of the sheet viscosity *versus* each of these quantities are included in the ESI,† however we note several notable features of these plots in the following discussion.

In Fig. 7, we plot these three summary statistics as a function of $\chi^{-1}$ and $K$ to explain the observed rheological behavior.

**4.2.1 Folded: low $\chi^{-1} \lesssim 1.4 \times 10^2$, low $K \lesssim 3.0$ behavior.** In this regime, sheets are 1D or 2D folded. Below $\chi^{-1} \sim 1.4 \times 10^1$, $R_g/L$ and $\zeta^2$ increase with shear rate. This corresponds to fewer sheets adopting the 2D folded conformation at higher shear rates. However, at even higher $\chi^{-1}$, these values plateau despite shear-thinning continuing. Peculiarly, there appears to be no strong correlation between radius of gyration and sheet

viscosity for folded sheets. Instead, the 1D folded sheets form two distinct clusters, one with a higher sheet viscosity ($\sim 0.35 \times 6\pi\eta\dot{\gamma}L^3$) and one with a lower sheet viscosity ($\sim 0.2 \times 6\pi\eta\dot{\gamma}L^3$).

This can be explained by looking at the average alignment of the sheets, which increases with shear rate. For prolate spheroids (ellipsoids with one large axis and two small axes) such as the minimum bounding ellipsoid of 1D folded sheets, large average alignment ("log-rolling") behavior is favored, which is why large average alignments result in lower sheet viscosities. Conceptually, this is because the distance the sheet "sticks out" into the shear axis is lower. These two types of motions (high and low average alignment) were observed in the past as the long-time behavior for ellipsoidal particles in shear.[70]

Indeed, for 1D folded sheets, most sheets have an average alignment close to either 1 or 0, indicating that they reach one of these terminal behaviors. The mechanism for these sheets deviating from their Jeffrey orbits to reach this high or low average alignment state is possibly the deformability of the sheets, which has been shown to influence the orbits sheets take in this manner.[71,72] 1D folded sheets with high average alignments have lower stresses than 1D folded sheets with low average alignments, explaining the two clusters observed in a scatter plot of sheet viscosity *versus* the $R_g/L$. The behavior of individual sheets is erratic, necessitating an average over initial condition. Thus, shear-thinning is due to a statistical average over many initial conditions. At higher shear rates, sheets on average adopt more log-rolling behavior, causing shear-thinning. This makes sense, as stronger shears cause greater perturbations in sheets, and thus allow for them to be more likely to be able to access the more favorable, lower stress, rotational behavior. Note that the decrease in average alignment at $\chi^{-1} \sim 1.4 \times 10^2$ is due to the rare appearance of tumbling sheets at this value of $\chi^{-1}$.

**4.2.2 Tumbling: high $\chi^{-1} \gtrsim 1.4 \times 10^2$, low $K \lesssim 3.0$ behavior.** Once shear increases enough to cross the tumbling/folded boundary, $R_g/L$ decreases slightly before recovering to close to the 1D folded value. $\zeta^2$ and the average alignment,
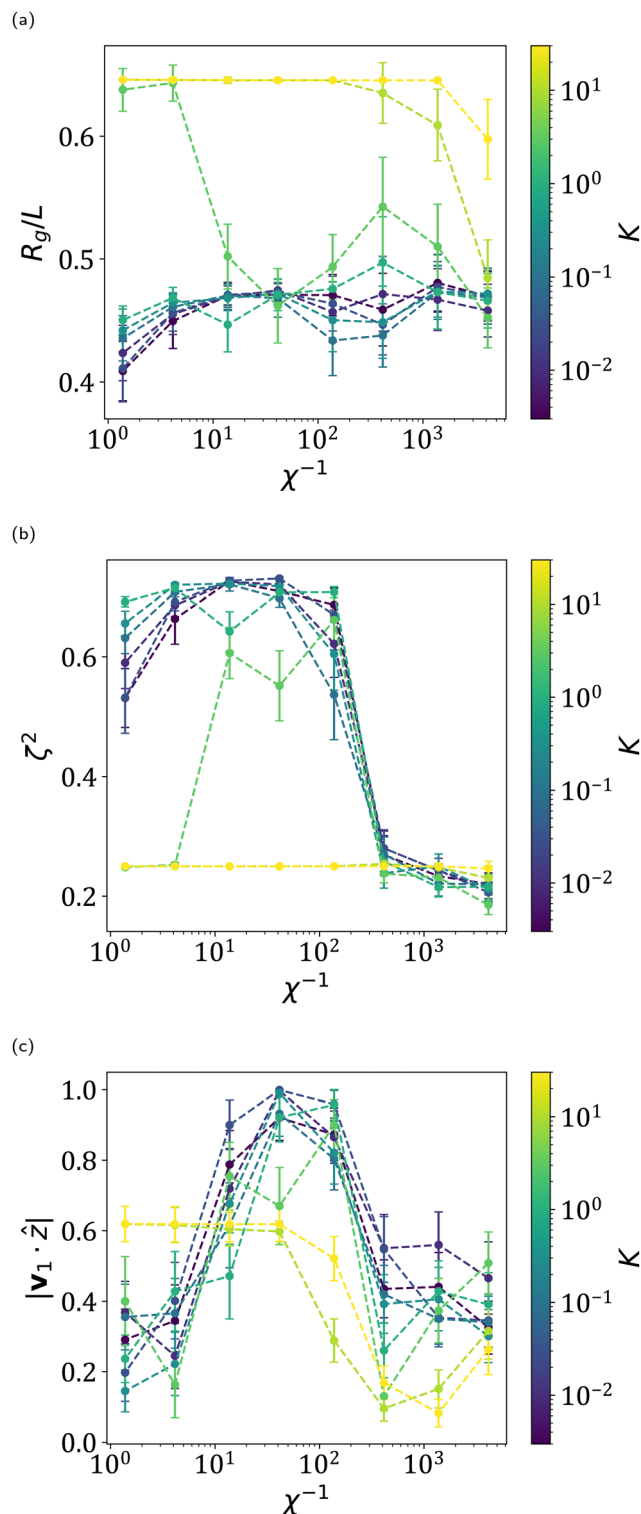
(a)



(b)

(c)

**Fig. 7** (a) Radius of gyration, (b) relative shape anisotropy, and (c) alignment averaged over the last $200\dot{\gamma}t$ and all $\phi$. Error bars are 95% confidence intervals. Dotted lines drawn to guide the eye.

however, both decrease drastically. While the trends for $R_{g}/L$ and the average alignment upon increasing $\chi^{-1}$ further are noisy and depend on the specific value of $K$, $\zeta^{2}$ continuously decreases with shear rate. Thus, shear thickening is caused by

sheets with lower values of $\zeta^{2}$ sticking out further into the shear axis at larger shear rates. This makes sense, as lower values of $\zeta^{2}$ correspond to more spherically symmetric sheets, where the effect of increasing average alignment on sheet viscosity is lower. Thus, the sheet viscosity is higher for the same values of $R_{g}/L$ and average alignment. Note that an average alignment value of approximately 0.52 corresponds to random orientation, which is around where the average alignments hover past the tumbling transition, suggesting that there is less preference for a particular rotational behavior. This is explained by the small values of $\zeta^{2}$.

Sheets exhibiting teacup behavior have similar sheet viscosities to folded sheets. This behavior is seen as a low sheet viscosity cluster of low average alignment tumbling sheets at a range of $R_{g}/L$. This behavior decreases in frequency at higher shear rates as it is a self-interaction-dependent behavior, which could contribute to the shear-thickening behavior. However, because this behavior is relatively rare, we expect that its effect is small. A detailed study of teacup behavior, its frequency as a function of $\chi^{-1}$ and $K$, and its effects on the sheet viscosity would be enlightening.

Another interesting aspect of tumbling sheets is their tumbling time, which is roughly the time for a sheet to make half a revolution about the vorticity axis. Scaling arguments for the tumbling time of 2D polymers have been proposed and confirmed with simulations for flipping sheets in previous work.[53] These scaling arguments are indeed only valid for relatively inflexible sheets. Because tumbling sheets are constantly deforming, it is difficult to both develop scaling arguments for the tumbling time as well as calculate it in simulations. This is further complicated by the existence of self-interactions in these sheets, which can change their effective macroscopic bending rigidities and affect their conformational behaviors. However, we believe that a detailed study on tumbling times for these sheets would be valuable and merits further investigation. Flipping times for folded sheets could likely be predicted using the average rotational velocity of its corresponding Jeffrey orbit. However, because the sheets are deformable, they are likely to adopt different trajectories according to an effective orbit constant and aspect ratio.[73] A study of the flipping dynamics of folded sheets was not conducted in this work, but would also be valuable in the future.

**4.2.3 Flat: high $K \gtrsim 3.0$ behavior.** For large enough values of $K$, bending rigidity overcomes interaction strength, and sheets are flat. The deviation from zero sheet viscosity, which would be the case for an infinitely thin sheet in the flow-vorticity plane, comes from a fraction of the flat sheets which lie in the flow-shear plane and rotate like a discus about the vorticity axis. Because these sheets stick out into the shear axis by the maximum amount possible for inextensible sheets, these sheets produce the highest sheet viscosities of any other conformational or rotational behavior. As shear increases, this behavior becomes less likely, again resulting in overall shear-thinning behavior. In Fig. 6, the sheet viscosity curves for low $\chi^{-1}$ and $K \geq 10.0$ are flat. To observe shear-thinning behavior here, we suspect that more initial conditions need to be

sampled. Past the tumbling transition, some sheets begin to tumble, resulting in shear-thickening as before.

The value of $K \sim 3.0$ appears to be right at the boundary between low $K$ and high $K$ behaviors and exhibits a mix of both behaviors, resulting in complex trends in $R_g/L$, $\zeta^2$, and average alignment.

In Fig. 6, we scale the sheet viscosity to $L^3$. However, given two additional length scales, $a$ and $\sigma$, this is not necessarily the proper scale. Furthermore, the proper scale for the sheet viscosity might be different for flat vs. tumbling vs. folded sheets. We have not confirmed any such scalings in this work, but we believe it warrants investigation and discuss predicted scalings in Appendix D.

Note that thermal energy would cause deviations from the discussed conformational behaviors which would decrease with increasing shear rate, likely resulting in the shear-thinning behavior seen in previous work.[54]

# 5 Conclusions

In this work, we examined the role of short-ranged attractive interactions for semi-flexible, athermal sheets in shear flow. We found a rich set of conformations which depend on two dimensionless groups: the material properties of the sheet ($K$) and experimental conditions ($\chi$). We characterized these sheets as flat, tumbling, 1D folded, or 2D folded based on the eigenvalues of the gyration tensor. We found roughly that sheets folded when $K \lesssim \mathcal{O}(1)$ and $\chi^{-1} \lesssim \mathcal{O}(10^2)$, tumbled when $K \lesssim \mathcal{O}(1)$ and $\chi^{-1} > \mathcal{O}(10^2)$, and were flat otherwise, although the exact behavior depended highly on initial condition near the boundaries.

We used the average signed local mean curvature of the sheets to show the nature of each type of sheet. Specifically, we identified parallel folds in 1D folded sheets and non-parallel folds in 2D folded sheets. We used a simple energetic argument to estimate the number of folds in a 1D folded sheet and showed that our equation matched well with the number of folds for these sheets in the low $K$ limit. We also showed the relevance of the bending rigidity to shear ($S$) in inducing folding when $K \sim 3$. From this, we proposed a mechanism of an initial buckling followed by shear-induced annealing towards the most energetically favorable number of folds. The strength of shear determines the degree of annealing which is possible. We also discussed the expected effect of changing $L$ on the rheological properties of the sheet based on the predicted number of folds in a 1D folded sheet.

Finally, we calculated an approximate upper-bound on the stresslet, which is expected to grow linearly with the viscosity of a dilute suspensions of these sheets. We found shear-thinning followed by shear-thickening behavior with increasing shear rate, with different behavior depending on whether $K$ is greater than or less than 1. This shear-thinning is present in the absence of sheet-sheet interactions and thermal fluctuations. Instead, it is a result of the average conformational and rotational behaviors of folded sheets. The changes in the conformation of a sheet with changing initial conditions follow trends, but are chaotic in the sense that small changes in the initial conformation can cause unpredicted changes in the final conformation near the boundaries between different conformations, similar to previous work.[53] We have yet to study the effect of changes in $\theta$, the initial orientation of the sheet about the vorticity axis.

We note here that thermal fluctuations cause out-of-plane stiffening for sheets,[20,22,58,74] which can change their bending rigidity quite significantly. Translating this work from the athermal limit to real systems, therefore, requires careful consideration of the effective bending rigidity of the system.

This type of shear-thinning into shear-thickening behavior is often attributed to the buildup and breakdown of agglomerates or other multi-sheet structures. However, we show that even in the dilute limit, this behavior can still emerge.

# Author contributions

William T. Funkenbusch – methodology, investigation, visualization & writing. Kevin S. Silmore – methodology & writing. Patrick S. Doyle – supervision & writing.

# Conflicts of interest

There are no conflicts to declare.

# Appendices

## Appendix A: neglecting lubrication forces

As parallel sections of sheet approach each other, a lubrication force is generated. Consider two parallel sections of sheet of area, $A$, approaching due to shear and initially separated by a distance, $2\sigma$. The strongest lubrication forces will be generated when the characteristic length of these sheet sections is $L$. The lubrication force goes as the lubrication pressure, $p_{lub}$, times the area of the sheet sections:

$$F_{lub} \sim p_{lub}A. \tag{10}$$

The scaling for $p_{lub}$ can be obtained from the lubrication equation:

$$\frac{\partial p_{lub}}{\partial x} = \eta \frac{\partial^2 u}{\partial z^2}. \tag{11}$$

The $x$ direction goes laterally along the sheets and the $z$ direction goes perpendicularly from the sheets. Therefore, $dx \sim L$ and $dz \sim \sigma$. $u$ is the lateral velocity. The maximum relative velocity of the two sheet sections due to shear is $\sigma\dot{\gamma}$. The lateral velocity, to satisfy the continuity equation, thus goes as $u \sim L\dot{\gamma}$. Together,

$$F_{lub} \sim \frac{A\eta\dot{\gamma}L^2}{\sigma^2}. \tag{12}$$

The energetic benefit of bringing a bead from non-interacting to interacting with a neighboring sheet section goes as $\tilde{\varepsilon}\sigma^2$. The distance it must travel to go from non-interacting to

interacting goes as $\sigma$. In bringing two parallel sheet sections together, the number of beads which become interacting with the neighboring sheet section goes as $A/a^2$. Therefore, the force of interaction goes as

$$F_{\text{int}} \sim \tilde{\varepsilon}\sigma^2 \frac{1}{\sigma} \frac{A}{a^2}. \qquad (13)$$

Taking the ratio between the lubrication and interaction forces gives their relative strength:

$$\frac{F_{\text{lub}}}{F_{\text{int}}} \sim \frac{\eta\dot{\gamma}L^2 a^2}{\tilde{\varepsilon}\sigma^3}. \qquad (14)$$

Our simulations, which neglect lubrication forces, are valid when this ratio is much less than unity. For example, graphene has inter-atom separation, $a \sim \mathcal{O}\,(1\ \text{Å})$, and athermal Lennard Jones interaction strength, $\tilde{\varepsilon} \sim \mathcal{O}\,(0.1\ \text{eV Å})$ with interaction range $\sigma \sim \mathcal{O}\,(1\ \text{nm})$.[67] We use the above approximation for the lubrication force even though the continuum approximation breaks down at these length scales. This means that even at high shear rates, $\dot{\gamma} \sim \mathcal{O}\,(10^3\ \text{s}^{-1})$, lubrication forces are small for graphene sheets in water as long as the sheet size, $L \ll 10\ \mu\text{m}$. This is reasonable for the $\mathcal{O}\,(\mu\text{m})$ flakes produced by exfoliation techniques[75–77] and becomes better for smaller shear rates or larger interaction ranges. Furthermore, the repulsive nature of the Lennard–Jones interaction at small distances restricts sheet segments from getting too close, similarly to lubrication forces. For purely attractive potentials, lubrication forces could fill a similar role in restricting the distance between neighboring sheet segments. Thus, we believe our decision to neglect lubrication forces is valid for real systems.

## Appendix B: derivation of $\chi$

Consider 2 parallel sheets of characteristic size $L$ interacting *via* a short-ranged potential of range $\sigma$ and separated by their equilibrium distance, $\sigma$. If the sheets are sheared such that the flow-vorticity plane cuts between them, the shear force trying to separate the sheets can be approximated as

$$F_{\text{shear}} = 6\pi\eta a\sigma\dot{\gamma}N_{\text{beads}}, \qquad (15)$$

where $\sigma\dot{\gamma}$ is the relative velocity induced on the sheets due to shear ($6\pi\eta a\sigma\dot{\gamma}$ is the Stokes' drag on a sphere) and $N_{\text{beads}} \sim (L/a)^2$ is the number of beads in each sheet.

We now consider the force required to slide the sheets and break the short-ranged interactions between them. Assuming the sheet is large ($L \gg a$) and the separation is large ($\sigma \gg a$), the energy of the beads in the bulk of the sheet does not change as the sheets slide relative to each other – only beads which are at the leading and trailing edges of the slide matter. The number of beads which separate as a result of a slide of distance $\sigma$ can be approximated as

$$\Delta N_{\text{slide}} \sim \frac{L\sigma}{a^2}. \qquad (16)$$

The change in energy for each of these beads is approximately

$$\Delta E_{\text{bead}} \sim \tilde{\varepsilon}\sigma^2 \qquad (17)$$

Thus, the force required to separate the beads is approximately

$$F_{\text{slide}} \sim \frac{\Delta N_{\text{beads}}\Delta E_{\text{bead}}}{\sigma} = \tilde{\varepsilon}\sigma^2\left(\frac{L\sigma}{a^2}\right)\left(\frac{1}{\sigma}\right). \qquad (18)$$

Taking the ratio of these two forces gives the dimensionless parameter we desire to an order 1 geometry-, orientation-, and packing-specific constant:

$$\chi \equiv \frac{F_{\text{slide}}}{F_{\text{shear}}} \sim \frac{\tilde{\varepsilon}\sigma^2}{6\pi\eta\dot{\gamma}L^2\sigma}\left(\frac{L}{a}\right). \qquad (19)$$

## Appendix C: derivation and confirmation of $n^*_{\text{fold}}$ scaling

We wish to obtain an approximation for the optimal number of folds in a 1D folded sheet. We make the following simplifying assumptions. First, the folds are parallel and equally spaced across the length of the sheet, with regions of flat sheet between them. Second, only neighboring parallel sections of sheet will interact with each other (*i.e.* the interaction is short-ranged). Third, the sheet is rectangular with characteristic length $2L$ and characteristic width $2W$. Fourth, that there is no stretching or compression of the sheet (*i.e.* FvK $\gg 1$). We define $n_{\text{fold}}$ to be the number of folds in the sheet, $w_{\text{fold}}$ to be the width of a fold, and $w_{\text{flat}}$ to be the width of a flat region. With these assumptions, we obtain the following balance for the length of the sheet:

$$2L = n_{\text{fold}}w_{\text{fold}} + (n_{\text{fold}} + 1)w_{\text{flat}}. \qquad (20)$$

The energy of bending roughly goes as the number of triangles which are within folds times the bending rigidity,

$$E_{\text{bending}} \sim \kappa n_{\text{fold}}\left(\frac{Ww_{\text{fold}}}{2a^2}\right). \qquad (21)$$

The energy of interaction goes as

$$E_{\text{interaction}} \sim \tilde{\varepsilon}\sigma^2 n_{\text{fold}}\left(\frac{Ww_{\text{flat}}}{a^2} + \beta'\frac{Ww_{\text{fold}}}{2a^2}\right), \qquad (22)$$

where the first term sums interactions for beads between parallel regions and the second term sums interactions for beads within folds. The parameter $\beta'$ is a fold geometry-specific parameter added as a measure of the strength of interactions for beads within folds. We wish to minimize the quantity

$$E = \alpha'E_{\text{bending}} - E_{\text{interaction}} \qquad (23)$$

with respect to $n_{\text{fold}}$ to obtain the optimal number of folds, $n^*_{\text{fold}}$. The term $\alpha'$ is a fold geometry-specific parameter added as a measure of the relative strength of bending rigidity to interaction strength. Doing so, we obtain

$$n^*_{\text{fold}} \approx \sqrt{\frac{2L/w_{\text{fold}} + 1}{1 - \beta + \alpha K}} - 1, \qquad (24)$$

where $\alpha = \alpha'/2$ and $\beta = \beta'/2$ have been redefined for convenience. We note that the the characteristic width of the sheet, $2W$, disappears from the final equation as all interactions are linear
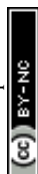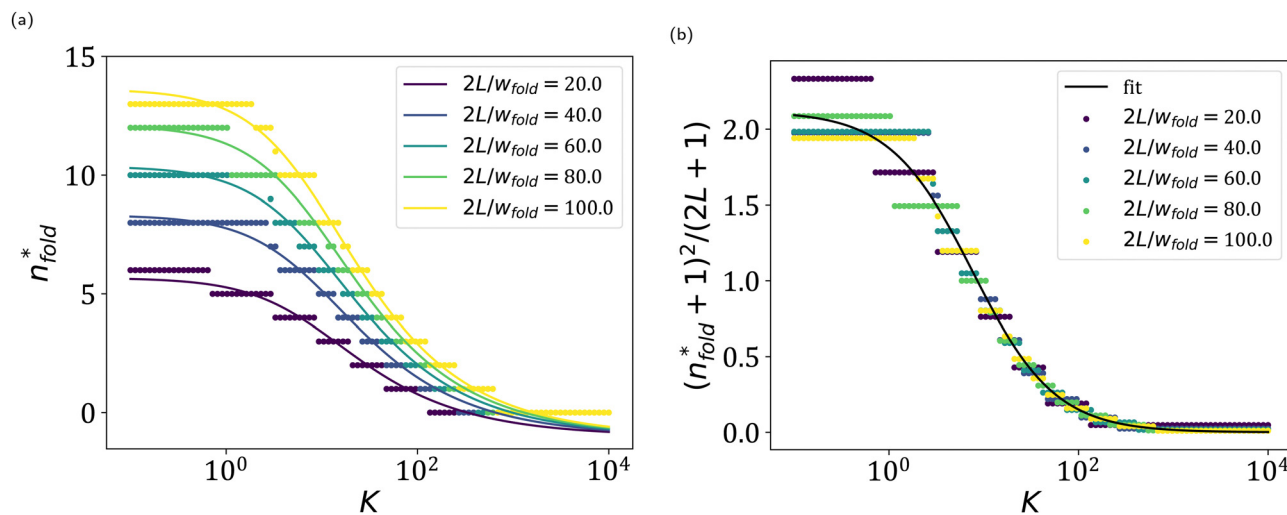
**Fig. 8** (a) Optimal number of folds for varying $K$ and $L/w_{fold}$. Points are data points and solid lines are eqn (24). Optimal values of $\alpha$ and $\beta$ were found to be $\alpha = 0.0618 \pm 0.0010$ and $\beta = 0.528 \pm 0.003$ ($\pm$ one standard deviation) using least-squares regression with $R^2 = 0.989$. (b) Master curve using eqn (24) to collapse all plots of $n^*_{\text{fold}}$.

in this term. For non-rectangular sheets which are wide enough such that edge effects are irrelevant (*i.e.* most beads are interior beads), the changing width affects the energy because folds and flat regions can be in locations with different widths. This effect is small for slowly-changing widths and thin folds and/or thin flat regions.

We confirm this scaling by generating rectangular sheets (such that each interior bead of these sheets has 6 neighbors) and finding their optimal number of folds. All neighboring beads in these sheets, even the ones in folds, are a constant distance, $2a$, apart, and neighboring parallel regions of sheet are a constant distance, $\sigma$, apart. We choose $w_{\text{fold}} = 6a$ and $\sigma = 4\sqrt{6}a/3$ for consistency with our simulations. A folded region consists of 1 row of beads within a flat region, 1 row at the "crease" of the fold, and 1 row within the neighboring flat region. We find the optimal number of folds for a given $K$ and $L/w_{\text{fold}}$ with constant $W/w_{\text{fold}} = 50.0$. We then fit these data to eqn (24) using least-squares regression, and find $\alpha = 0.0618 \pm 0.0010$ and $\beta = 0.528 \pm 0.003$ ($\pm$ one standard deviation). The fit can be seen in Fig. 8. This equation appears to fit the data quite well, with $R^2 = 0.989$. The data also collapse fairly well onto a master curve, with the largest deviation coming from the smallest sheet, where edge effects are the most relevant. This suggests that $n^*_{\text{fold}} \sim \sqrt{L/w_{\text{fold}}}$, as predicted.

## Appendix D: discussion of $L$ dependence of rheological properties

Because $w_{\text{fold}} \sim a$, where $a$ is the equivalent of a molecular or atomistic length scale in a 2D sheet, the number of folds is expected to increase for larger sheets, with $n^*_{\text{fold}} \sim (L/a)^{1/2}$, as derived in Appendix C. For a 1D folded sheet, its largest characteristic size scales as $L$ because this dimension is parallel to the folds. Another characteristic size is the width of each folds times the number of folds: $\sigma n_{\text{fold}} \sim \sigma(L/a)^{1/2}$. The last

characteristic size is the width of each flat region: $w_{\text{flat}} \sim L/n_{\text{fold}} \sim a(L/a)^{1/2}$. The sheet viscosity will grow roughly as the cross-sectional area of the sheet in the shear-vorticity plane times the length of the sheet along the shear axis. If the sheet is log-rolling, for example, its cross-sectional area in the shear-vorticity plane goes as $L^{3/2}$ and its length along the shear axis goes as $L^{1/2}$. The sheet viscosity would therefore go as $L^2$. Orientations of sheets with their largest dimension rotating about the vorticity plane have sheet viscosities which go as $L^{5/2}$. Rolled-up sheets occupy a roughly circular area perpendicular to their largest axis which goes as $L\sigma$, so its other characteristic sizes go as $\sqrt{L\sigma} \sim L^{1/2}$, so its sheet viscosity will have the same scaling as sheets with many folds. Assuming each characteristic size of a tumbling sheet scales with $L$, the stress scales as $L^3$, which is stronger than in the 1D folded regime.

If we were to treat $a$ as simply the smallest resolvable length scale in the system, we would expect $w_{\text{fold}}$ to grow proportionally to $L$. In this case, $n^*_{\text{fold}}$ is not a function of $L$, and the three characteristic sizes of the sheet grow as, from largest to smallest, $L$, $L$, and $\sigma$. In the limit of $L \gg \sigma$, the sheet will preferentially align itself with the flow-vorticity plane, and behave effectively as a flat sheet with a small width. The sheet viscosity, assuming the largest axis is aligned with the vorticity axis, would thus grow as $L\sigma^2$, which is weaker than when $a$ is the atomistic or molecular length scale in the system. This highlights the importance of treating $a$ as an explicit length scale in these systems.

As $L$ increases, $\chi^{-1}$ increases, and sheets are pushed toward the tumbling regime. Sheet suspensions are often polydisperse[78] and the total contribution to the viscosity in a dilute suspension is the sum of the individual sheet viscosities. So, the total contribution to the viscosity is a weighted sum of the sheet viscosity from each particle size's sheet viscosity, each of which is non-monotonic with shear rate.

# Appendix E: movies

Movies of sheet trajectories can be found in the ESI† and include trajectories for flat, tumbling, 1D folded, and 2D folded sheets. They also include trajectories for a sheet with a low average alignment (1D folded), a sheet exhibiting teacup behavior (tumbling), and a rolled-up sheet (1D folded). All trajectories are accompanied by movies of the corresponding signed local mean curvatures of the sheets. Sheet trajectories were rendered in Ovito.[65]

# Acknowledgements

# Notes and references

1 Y. Xu, H. Cao, Y. Xue, B. Li and W. Cai, *Nanomaterials*, 2018, **8**, 942.

2 J. Stafford, A. Patapas, N. Uzo, O. K. Matar and C. Petit, *AIChE J.*, 2018, **64**, 3246–3276.

3 A. Amiri, M. Naraghi, G. Ahmadi, M. Soleymaniha and M. Shanbedi, *FlatChem*, 2018, **8**, 40–71.

4 A. Ambrosi and M. Pumera, *Chem. Soc. Rev.*, 2018, **47**, 7213–7224.

5 J. N. Coleman, M. Lotya, A. O'Neill, S. D. Bergin, P. J. King, U. Khan, K. Young, A. Gaucher, S. De and R. J. Smith, *et al.*, *Science*, 2011, **331**, 568–571.

6 V. Nicolosi, M. Chhowalla, M. G. Kanatzidis, M. S. Strano and J. N. Coleman, *Science*, 2013, **340**, 1226419.

7 E. Varrla, C. Backes, K. R. Paton, A. Harvey, Z. Gholamvand, J. McCauley and J. N. Coleman, *Chem. Mater.*, 2015, **27**, 1129–1139.

8 R. Jha and P. K. Guha, *J. Mater. Sci.*, 2017, **52**, 7256–7268.

9 T. Gibaud, C. N. Kaplan, P. Sharma, M. J. Zakhary, A. Ward, R. Oldenbourg, R. B. Meyer, R. D. Kamien, T. R. Powers and Z. Dogic, *Proc. Natl. Acad. Sci. U. S. A.*, 2017, **114**, E3376–E3384.

10 F. Ding, J. Liu, S. Zeng, Y. Xia, K. M. Wells, M.-P. Nieh and L. Sun, *Sci. Adv.*, 2017, **3**, e1701212.

11 G. Shao, Y. Lu, F. Wu, C. Yang, F. Zeng and Q. Wu, *J. Mater. Sci.*, 2012, **47**, 4400–4409.

12 F. Tardani, W. Neri, C. Zakri, H. Kellay, A. Colin and P. Poulin, *Langmuir*, 2018, **34**, 2996–3002.

13 P. Davidson, C. Penisson, D. Constantin and J.-C. P. Gabriel, *Proc. Natl. Acad. Sci. U. S. A.*, 2018, **115**, 6662–6667.

14 A. Laskar, O. E. Shklyaev and A. C. Balazs, *Sci. Adv.*, 2018, **4**, eaav1745.

15 C. Kamal, S. Gravelle and L. Botto, *Nat. Commun.*, 2020, **11**, 2425.

16 A. R. Klotz, B. W. Soh and P. S. Doyle, *Proc. Natl. Acad. Sci. U. S. A.*, 2020, **117**, 121–127.

17 P. Liu, A. T. Liu, D. Kozawa, J. Dong, J. F. Yang, V. B. Koman, M. Saccone, S. Wang, Y. Son and M. H. Wong, *et al.*, *Nat. Mater.*, 2018, **17**, 1005–1012.

18 B. Tang, Z. Xiong, X. Yun and X. Wang, *Nanoscale*, 2018, **10**, 4113–4122.

19 B. Tang, E. Gao, Z. Xiong, B. Dang, Z. Xu and X. Wang, *Chem. Mater.*, 2018, **30**, 5951–5960.

20 D. Nelson, T. Piran and S. Weinberg, *Statistical mechanics of membranes and surfaces*, World Scientific, 2004.

21 Y. Kantor and D. R. Nelson, *Phys. Rev. Lett.*, 1987, **58**, 2774.

22 D. Nelson and L. Peliti, *J. Phys.*, 1987, **48**, 1085–1092.

23 B. Duplantier, *Phys. Rev. Lett.*, 1987, **58**, 2733.

24 M. Paczuski, M. Kardar and D. R. Nelson, *Phys. Rev. Lett.*, 1988, **60**, 2638.

25 E. Frey and D. R. Nelson, *J. Phys. I*, 1991, **1**, 1715–1757.

26 M. J. Bowick and A. Travesset, *Phys. Rep.*, 2001, **344**, 255–308.

27 A. Košmrlj and D. R. Nelson, *Phys. Rev. B*, 2016, **93**, 125431.

28 M. J. Bowick, A. Košmrlj, D. R. Nelson and R. Sknepnek, *Phys. Rev. B*, 2017, **95**, 104109.

29 Y. Kantor, M. Kardar and D. R. Nelson, *Phys. Rev. A: At., Mol., Opt. Phys.*, 1987, **35**, 3056.

30 M. Kardar and D. R. Nelson, *Phys. Rev. Lett.*, 1987, **58**, 1289.

31 M. Plischke and D. Boal, *Phys. Rev. A: At., Mol., Opt. Phys.*, 1988, **38**, 4943.

32 F. F. Abraham, W. Rudge and M. Plischke, *Phys. Rev. Lett.*, 1989, **62**, 1757.

33 J.-S. Ho and A. Baumgärtner, *Phys. Rev. Lett.*, 1989, **63**, 1324.

34 F. F. Abraham and D. R. Nelson, *Science*, 1990, **249**, 393–397.

35 F. F. Abraham and D. R. Nelson, *J. Phys.*, 1990, **51**, 2653–2672.

36 G. S. Grest and I. B. Petsche, *Phys. Rev. E: Stat. Phys., Plasmas, Fluids, Relat. Interdisc. Top.*, 1994, **50**, R1737.

37 M. J. Bowick, A. Cacciuto, G. Thorleifsson and A. Travesset, *Eur. Phys. J. E: Soft Matter Biol. Phys.*, 2001, **5**, 149–160.

38 R. Chianelli, E. Prestridge, T. Pecoraro and J. DeNeufville, *Science*, 1979, **203**, 1105–1107.

39 T. Hwa, E. Kokufuta and T. Tanaka, *Phys. Rev. A: At., Mol., Opt. Phys.*, 1991, **44**, R2235.

40 X. Wen, C. W. Garland, T. Hwa, M. Kardar, E. Kokufuta, Y. Li, M. Orkisz and T. Tanaka, *Nature*, 1992, **355**, 426–428.

41 M. Spector, E. Naranjo, S. Chiruvolu and J. Zasadzinski, *Phys. Rev. Lett.*, 1994, **73**, 2867.

42 S. B. Babu and H. Stark, *Eur. Phys. J. E: Soft Matter Biol. Phys.*, 2011, **34**, 1–7.

43 D. Liu and M. Plischke, *Phys. Rev. A: At., Mol., Opt. Phys.*, 1992, **45**, 7139.

44 P. Li, S. Wang, F. Meng, Y. Wang, F. Guo, S. Rajendran, C. Gao, Z. Xu and Z. Xu, *Macromolecules*, 2020, **53**, 10421–10430.

45 F. F. Abraham and M. Kardar, *Science*, 1991, **252**, 419–422.

46 Y. Xu and M. J. Green, *J. Chem. Phys.*, 2014, **141**, 024905.

47 Y. Xu and M. J. Green, *J. Polym. Sci., Part B: Polym. Phys.*, 2015, **53**, 1247–1253.

48 Y. Yu and M. D. Graham, *Soft Matter*, 2021, **17**, 543–553.

49 Y. Yu and M. D. Graham, *Phys. Rev. Fluids*, 2022, **7**, 023601.

50 G. Salussolia, C. Kamal, J. Stafford, N. Pugno and L. Botto, *Phys. Fluids*, 2022, **34**, 053311.

51 N. Lindahl, D. Midtvedt, J. Svensson, O. A. Nerushev, N. Lindvall, A. Isacsson and E. E. Campbell, *Nano Lett.*, 2012, **12**, 3526–3531.

52 H. Perrin, H. Li and L. Botto, *Phys. Rev. Fluids*, 2023, **8**, 124103.

53 K. S. Silmore, M. S. Strano and J. W. Swan, *Soft Matter*, 2021, **17**, 4707–4718.

54 K. S. Silmore, M. S. Strano and J. W. Swan, *Soft Matter*, 2022, **18**, 768–782.

55 G. B. Jeffery, *Proc. R. Soc. London, Ser. A*, 1922, **102**, 161–179.

56 X. Zhang, Y. Tang, X. Wang, J. Zhang, D. Guo and X. Zhang, *J. Polym. Environ.*, 2018, **26**, 3502–3510.

57 Y. H. Shim, H. Ahn, S. Lee, S. O. Kim and S. Y. Kim, *ACS Nano*, 2021, **15**, 13453–13462.

58 P. Liu and Y. Zhang, *Appl. Phys. Lett.*, 2009, **94**, 231912.

59 J.-W. Jiang, Z. Qi, H. S. Park and T. Rabczuk, *Nanotechnology*, 2013, **24**, 435705.

60 P. Poulin, R. Jalili, W. Neri, F. Nallet, T. Divoux, A. Colin, S. H. Aboutalebi, G. Wallace and C. Zakri, *Proc. Natl. Acad. Sci. U. S. A.*, 2016, **113**, 11088–11093.

61 G. Gompper and D. Kroll, *J. Phys. I*, 1996, **6**, 1305–1320.

62 J. Rotne and S. Prager, *J. Chem. Phys.*, 1969, **50**, 4831–4837.

63 J. A. Anderson, J. Glaser and S. C. Glotzer, *Comput. Mater. Sci.*, 2020, **173**, 109363.

64 A. M. Fiore, F. Balboa Usabiaga, A. Donev and J. W. Swan, *J. Chem. Phys.*, 2017, **146**, 124116.

65 A. Stukowski, *Modell. Simul. Mater. Sci. Eng.*, 2009, **18**, 015012.

66 L. Liu, Z. Shen, M. Yi, X. Zhang and S. Ma, *RSC Adv.*, 2014, **4**, 36464–36470.

67 G. Klimchitskaya and V. Mostepanenko, *Phys. Rev. B: Condens. Matter Mater. Phys.*, 2013, **87**, 075439.

68 G. Batchelor, *J. Fluid Mech.*, 1970, **41**, 545–570.

69 S. Kim and S. J. Karrila, *Microhydrodynamics: principles and selected applications*, Courier Corporation, 2013.

70 G. I. Taylor, *Proc. R. Soc. London, Ser. A*, 1923, **103**, 58–61.

71 T. Omori, Y. Imai, T. Yamaguchi and T. Ishikawa, *Phys. Rev. Lett.*, 2012, **108**, 138102.

72 H. Zhao and E. S. Shaqfeh, *J. Fluid Mech.*, 2013, **725**, 709–731.

73 X. Zhang, W. A. Lam and M. D. Graham, *Phys. Rev. Fluids*, 2019, **4**, 043103.

74 A. Fasolino, J. Los and M. I. Katsnelson, *Nat. Mater.*, 2007, **6**, 858–861.

75 K. R. Paton, E. Varrla, C. Backes, R. J. Smith, U. Khan, A. O'Neill, C. Boland, M. Lotya, O. M. Istrate and P. King, *et al.*, *Nat. Mater.*, 2014, **13**, 624–630.

76 U. Khan, A. O'Neill, H. Porwal, P. May, K. Nawaz and J. N. Coleman, *Carbon*, 2012, **50**, 470–475.

77 J.-Y. Moon, M. Kim, S.-I. Kim, S. Xu, J.-H. Choi, D. Whang, K. Watanabe, T. Taniguchi, D. S. Park and J. Seo, *et al.*, *Sci. Adv.*, 2020, **6**, eabc6601.

78 J. Amaro-Gahete, A. Bentez, R. Otero, D. Esquivel, C. Jiménez-Sanchidrián, J. Morales, Á. Caballero and F. J. Romero-Salguero, *Nanomaterials*, 2019, **9**, 152.